Limits of the potential flow approach to the single-mode Rayleigh-Taylor problem

P. Ramaprabhu* and Guy Dimonte
Los Alamos National Laboratory, Los Alamos, New Mexico 87545, USA

Yuan-Nan Young
Department of Mathematical Sciences, New Jersey Institute of Technology, Newark, New Jersey 07102, USA

A. C. Calder
University of Chicago, Chicago, Illinois 60637, USA

B. Fryxell
Los Alamos National Laboratory, Los Alamos, New Mexico 87545, USA

(Received 9 May 2006; revised manuscript received 9 August 2006; published 20 December 2006)

We report on the behavior of a single-wavelength Rayleigh-Taylor flow at late times. The calculations were performed in a long square duct ($\lambda \times \lambda \times 8\lambda$), using four different numerical simulations. In contradiction with potential flow theories that predict a constant terminal velocity, the single-wavelength Rayleigh-Taylor problem exhibits late-time acceleration. The onset of acceleration occurs as the bubble penetration depth exceeds the diameter of bubbles, and is observed for low and moderate density differences. Based on our simulations, we provide a phenomenological description of the observed acceleration, and ascribe this behavior to the formation of Kelvin-Helmholtz vortices on the bubble-spike interface that diminish the friction drag, while the associated induced flow propels the bubbles forward. For large density ratios, the formation of secondary instabilities is suppressed, and the bubbles remain terminal consistent with potential flow models.

DOI: 10.1103/PhysRevE.74.066308 PACS number(s): 47.20.Bp

I. INTRODUCTION

The acceleration of a fluid into a second fluid of greater density ($\rho_2 > \rho_1$) produces the Rayleigh-Taylor (RT) instability [1], a problem of significance to the inertial confinement process [2], and supernovae explosions [3]. Small perturbations of amplitude h_0 and wave number $k=2\pi/\lambda$ at the interface between the fluids grow exponentially in time until $kh_0 \sim 1$

$$h(t) = h_0 \cosh(\Gamma t). \tag{1}$$

In the absence of surface tension, viscosity, or other mitigating effects, the associated growth rate [4] is $\Gamma = \sqrt{Agk}$, where g is the acceleration and the Atwood number $A = \frac{\rho_2 - \rho_1}{\rho_2 + \rho_1}$ parametrizes the density difference between the fluids. At larger amplitudes, the flow is differentiated into *bubbles* of light fluid rising into the heavy, and spikes, which are fingers of the heavy fluid descending into the light fluid. Drag-buoyancy [5] models and potential flow theory [6] predict that for $kh_0 > 1$, the perturbations undergo a nonlinear saturation toward a terminal bubble velocity given by

$$v_b = \mathrm{Fr}\sqrt{Ag\lambda/(1+A)}, \tag{2}$$

where Fr is the bubble Froude number. Numerical simulations [7] have shown that (2) holds for bubbles for all A, with Fr=0.56 for a square mode initial perturbation. The models also give corresponding expressions for spike behavior, although at large density differences, spikes do not stay terminal, but approach free fall ($h_s \sim 0.5gt^2$). Thus, bubble and spike growths are identical at small A, but diverge as $A \to 1$.

This simple picture of single-wavelength growth is significant because it can be extended through dimensional arguments to improve our understanding of the turbulent RT. Indeed, the so-called bubble competition [8] models treat dominant bubbles in a chaotic bubble front as essentially "single modes" isolated from the effects of neighbors. Such dominant bubbles grow self-similarly with their diameter $D_b \sim \lambda \propto h_b$, according to experiments and simulations. Thus, replacing $D_b(\lambda)$ with h_b for leading bubbles in (2), we get

$$h_b = \alpha A g t^2, \tag{3}$$

where α is the growth constant. Experiments [9] obtain $\alpha \sim 0.05$ and $D_b/h_b \sim (1+A)/4$ whereas simulations [10] report $\alpha \sim 0.03-0.09$ depending on the initial conditions.

The importance of the single-mode behavior can be quantified by inserting the self-similarity condition into Eq. (2). Then, for a constant D_b/h_b, the solution is given by Eq. (3) with

$$\alpha = \frac{\mathrm{Fr}^2}{8}\frac{\rho_1 + \rho_2}{\rho_2}\frac{D_b}{h_b}. \tag{4}$$

However, as described by [9–12], a value of Fr$\sim$1 is required to match the measured values of α and D_b/h_b, which is larger than the value Fr$\sim$0.56 calculated from potential flow. Analysis of leading bubbles from numerical simulations and experiments that accounts for the entrainment of the heavier fluid by bubbles confirm this higher value of Fr. Thus, leading bubbles in a turbulent flow resemble the isolated buoyant plumes of Scorer's experiment [13] (Fr=1.1),

*Center for Nonlinear Studies.

rather than an array of tightly packed bubbles (Fr=0.56). Such isolated plumes/bubbles have an increased Fr due to reduced counterflow drag from spike flow surrounding the bubbles—as the area separating neighboring bubbles is increased, the spike velocity is diminished due to mass conservation. This is evident in the experiments of [14], who observed an increase in the value of Fr of a lenticular bubble from $\frac{1}{2}$ to $\frac{2}{3}$, as the walls of the container were moved away. Similarly, the observed aspect ratios (D_b/h_b) of turbulent RT bubbles range from $\frac{1}{3}$ to $\frac{2}{3}$, in contrast to the single-mode value of ~ 1.

Thus, the single-mode description of leading bubbles in turbulent RT is promising, but must be revised towards a higher Fr and lower D_b/h_b. Simulations and experiments of single-wavelength RT flows [7,15] have focused on bubble evolution at early and intermediate times. In this paper, we use three-dimensional (3D) numerical simulations to study the late-time single-mode RT problem in a regime of relevance to the turbulent flow, i.e., with $h_b \sim 2-4D_b$. Under these conditions, the single-wavelength flow, much to our surprise, exhibits deviations from the expected terminal velocity. Bubbles (and spikes at low A) accelerate before approaching a Fr~ 1, closer to the turbulent value. We provide a phenomenological description of our observations, and an explanation for the late-time bubble acceleration.

II. NUMERICAL TECHNIQUES AND PROBLEM SETUP

The numerical algorithms used in this study have been described in detail in [16], and only a brief overview is provided here. Three of the numerical codes used the MILES (monotone integrated large eddy simulation) technique, while the fourth was a direct numerical simulation (DNS). RTI-3D [17] is a multiphase, incompressible, Eulerian solver and uses Van Leer flux limiters to prevent nonphysical oscillations. FLASH [18] and PROMETHEUS [19] solve the compressible Euler equations using the piecewise parabolic method on a 3D Cartesian grid. FLASH is a parallel code and has the added feature of adaptive mesh refinement, handled by the PARAMESH [20] library of routines. NAV/STK is a finite-volume solver for the full Navier-Stokes equations with a physical viscosity, in addition to the capability to handle surface tension effects. The MILES algorithm has an implicit viscosity due to subgrid smoothing of fine scales that may be written from dimensional arguments [16] as

$$\nu \sim \sqrt{Ag\Delta^3}, \tag{5}$$

where Δ is the zone size. It has been demonstrated that the numerical viscosity in these codes behaves much like a physical viscosity, not only giving the correct linear growth rates (modified by viscosity), but accurately predicting the Kolmogorov cutoff wave number in turbulent calculations [16]. In this work, we have performed additional tests to characterize the behavior of the numerical viscosity in the MILES codes, and these are described in the Appendix. Table I provides a summary of the numerical techniques discussed above.

TABLE I. Description of numerical codes used in this study.

	Governing equations	AMR	Surface tension	Compressible
RTI-3D	Euler	No	No	No
FLASH	Euler	Yes	No	Yes
NAV/STK	Navier-Stokes	Yes	Yes	No
PROMETHEUS	Euler	No	No	Yes

The three-dimensional simulations were initialized with a square-mode initial perturbation of amplitude h_0 and wave number k, of the form

$$h(x,y) = h_0\{\cos(kx) + \cos(ky)\}. \tag{6}$$

This form of the perturbation places the bubble at the center of the computational domain, while the spikes are placed at the corners. The perturbation amplitudes were chosen to be such that $kh_0 \ll 1$. To study the late-time behavior of RT, the perturbations were set up in a long, square duct ($\lambda \times \lambda \times 8\lambda$), with periodic boundary conditions in the lateral directions, and no-flow boundary conditions in the direction of gravity. The perturbation wavelengths, Atwood numbers used, and grid resolutions employed in the codes are listed in Table II. The compressible codes were run in a nearly incompressible limit, with an adiabatic condition [16] for the vertical density profile to approximate hydrostatic equilibrium.

TABLE II. Simulation parameters used in this study.

	Atwood number	Perturbation wavelength (cm)	Gravity (cm/s^2)	Resolution
RTI-3D	0.005	10.0	2.0	$32\times32\times256$
	0.1			
	0.25			
	0.5			
	0.75			
	0.9			
FLASH	0.1	0.25	1.0	128^*128^*1024
	0.25			
	0.5			
	0.9			
NAV/STK	0.1			48^*48^*384,
	0.2	1.0	1.0	64^*64^*512
	0.3			
	0.4			
	0.5			
	0.6			
	0.7			
	0.8			
	0.9			
PROMETHEUS	0.5	0.25	1.0	60×720

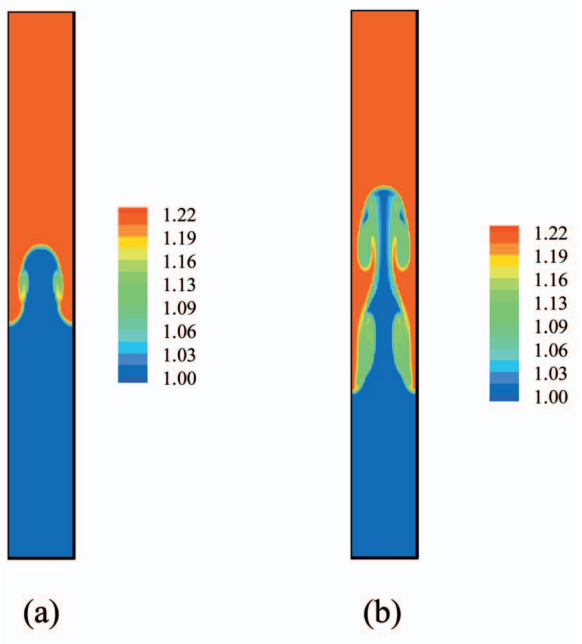

FIG. 1. (Color) Images of bubble front at early time (during terminal velocity) and late time (acceleration stage) from RTI-3D. $A=0.1$. Contour levels shown are in gm/cm^3.

The background pressure is chosen to be 500 dynes/cm^2, limiting the vertical density variation to less than 6%.

III. COMPUTATIONAL RESULTS

Figures 1 and 2 are contour plots of density $\left(\frac{\rho_1+\rho_2}{2}\right)$ from RTI-3D and NAV/STK simulations at $A=0.1$ and 0.2, respectively. The panel (a) is at an early-time while (b) is towards the end of the simulation. The realizations are in a plane passing through the center of the bubble, while the spikes are located outside this plane and near the corners of the box. The time histories of bubble amplitude and velocity from RTI-3D are shown in Figs. 3(a) and 3(b), respectively, at $A=0.5$. For $h_b/D_b<1$, bubble velocities are constant and in agreement with (2). As bubbles exceed this aspect ratio, they accelerate, before approaching a higher Fr late in time.

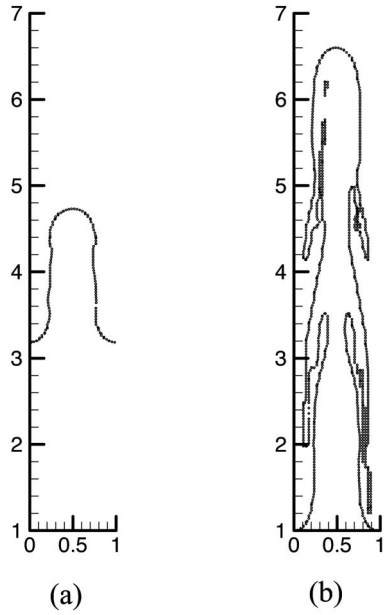

FIG. 2. Images of bubble front at early time (during terminal velocity) and late time (acceleration stage) from DNS. $A=0.2$. Location of original interface is at $y=4$ cm.

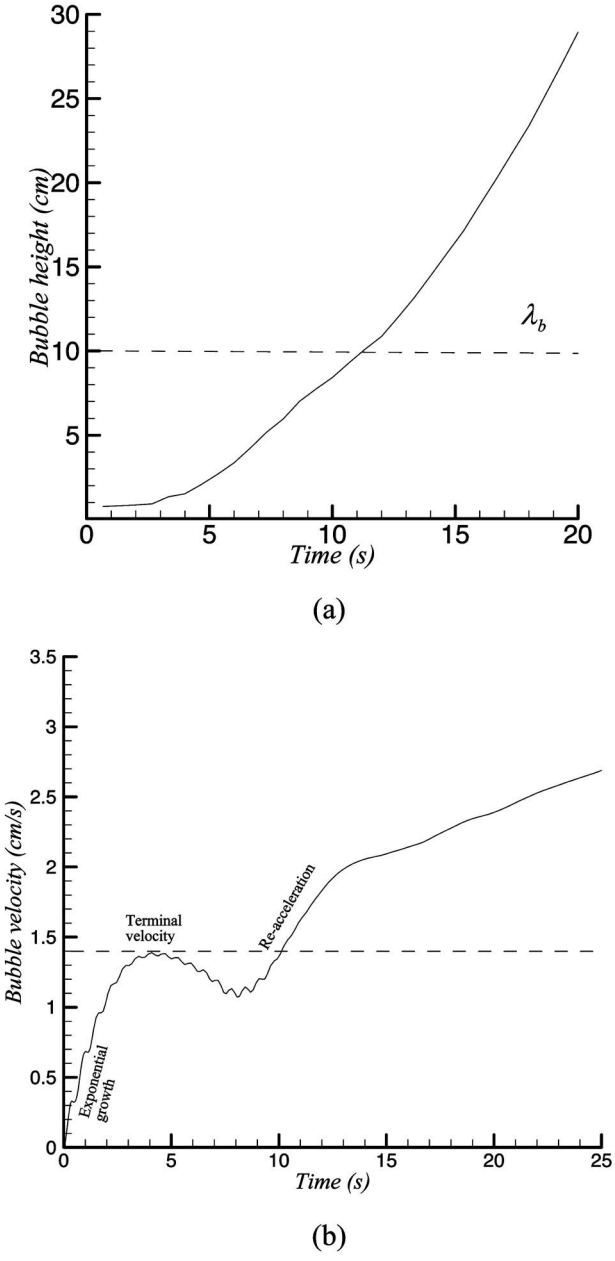

FIG. 3. Time histories of (a) bubble penetration and (b) bubble velocity showing distinct stages of single-wavelength bubble growth. Results shown are from RTI-3D at $A=0.5$. The dashed line in (a) represents the bubble wavelength λ_b, beyond which the reacceleration is observed. The terminal velocity from potential flow theory is included in (b) for comparison.

Figure 4 summarizes the variation of Fr with A for mildly nonlinear bubbles ($h_b \leqslant D_b$) from the MILES and DNS

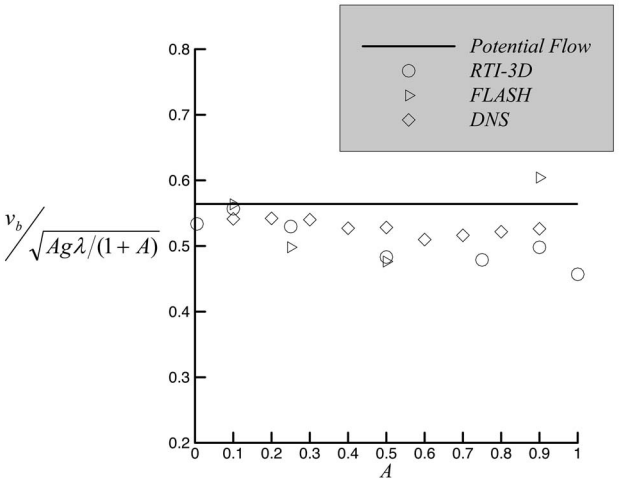

FIG. 4. Bubble Froude number $[v_b/\sqrt{Ag\lambda/(1+A)}]$ for $h_b/D_b<1$ at different Atwood numbers from numerical simulations and potential flow theory [6].

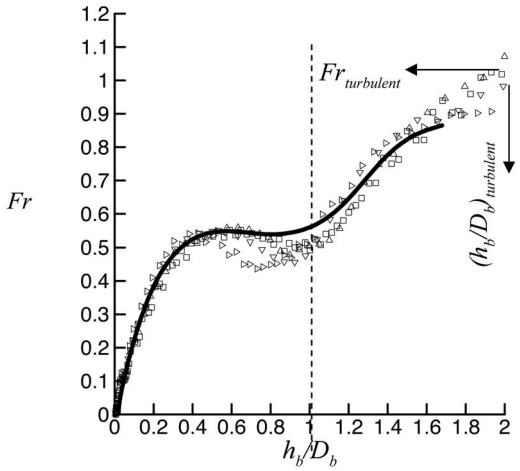

FIG. 5. Froude number $[v_b/\sqrt{Ag\lambda/(1+A)}]$ vs h_b/D_b from numerical simulations. Hollow symbols represent MILES, while the solid line indicates DNS. All calculations are for $A\leqslant 0.5$ and show onset of bubble acceleration at $\frac{h_b}{D_b}\sim 1$.

codes, and it shows agreement with the drag-buoyancy [5] and potential flow [6] type models. Note that the models assume a Bessel function for the initial interfacial perturbation, while our calculations are initialized with a square mode. This difference in the form of the perturbation does not lead to a discrepancy in the results. In this regime, bubbles have a Fr of 0.56, independent of A. For bubbles, balancing the buoyancy and drag forces gives

$$\ddot{h}_b = Ag - C\dot{h}_b^2 \frac{\rho_2}{\rho_1+\rho_2}\frac{\text{Area}}{\text{Volume}}, \tag{7}$$

where C is a drag coefficient. Choosing $C\sim 2\pi$ as suggested by [5], Area/Volume$\sim 1/D_b$, and setting $\ddot{h}_b=0$, we obtain (2) for v_b. This simple model ignores the late-time onset of secondary instabilities in the form of Kelvin-Helmholtz rollups at low A, and bubble-spike coupling at high A. A similar force balance analysis for spikes reveals identical spike behavior at low A. However, for $A>0.5$, the drag forces due to bubbles vanish, causing the spikes to accelerate [7], ultimately approaching free-fall $(h_s=\frac{1}{2}gt^2)$ as $A\to 1$. Note that this is in agreement with the recent calculations of [21], who use boundary-integral methods to investigate the late-time behavior of the single-mode RT flow at infinite density ratios.

According to Fig. 3, Eq, (7) describes the bubble behavior only up to intermediate times, but not the late-time acceleration and a possible asymptotic velocity saturation. This deviation from (7) is observed consistently in all of the numerical simulations shown in Fig. 5, which is a plot of the Froude number variation with bubble aspect ratio (h_b/D_b). Furthermore, the simulations consistently show that the onset of bubble acceleration is at $h_b/D_b\sim 1$, and that bubbles ultimately appear to approach Fr~ 1. However, it is not conclusive from Figs. 3(b) or 5 that there is a saturation observed at Fr~ 1, and if it is more stable than the first saturation at Fr ~ 0.56. We expect higher aspect ratio calculations will resolve this uncertainty. We note that in all the codes, this behavior is observed for $A<0.75$, and not at higher density differences. This is evident from the high Atwood cases shown in Fig. 6, which do not show any bubble acceleration late in time. A complete discussion of this Atwood number effect is deferred until Sec. IV. The marker arrows in Fig. 5 point to the turbulent values of Fr and h_b/D_b, obtained from simulations and experiments, for comparison.

Such late-time nonstationary behavior of single-mode RT spikes and bubbles were observed and reported in [22], who ascribe the deviation from steady state to changes in the tip curvature of bubbles and spikes. We argue in the following that it is the formation of secondary instabilities rather than the curvature of the bubble/spike tip that describes the observed behavior. The onset of bubble oscillations may also be observed at late-time in the two-dimensional (2D) DNS of [23]. Finally, 2D and 3D numerical simulations using the

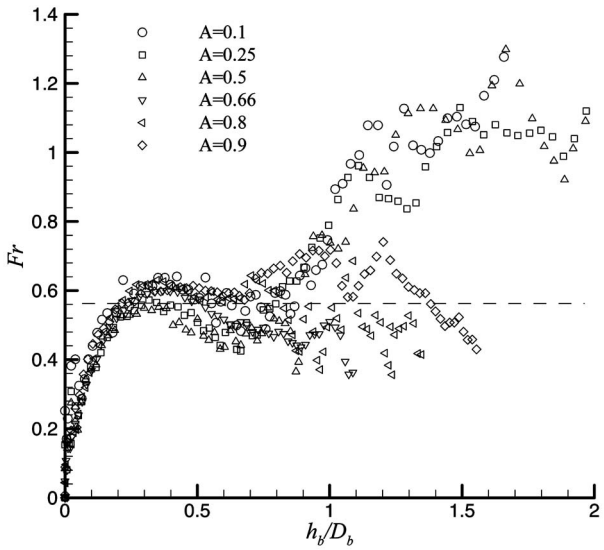

FIG. 6. Froude number $[v_b/\sqrt{Ag\lambda/(1+A)}]$ vs h_b/D_b from numerical simulations using the FLASH code at different A.

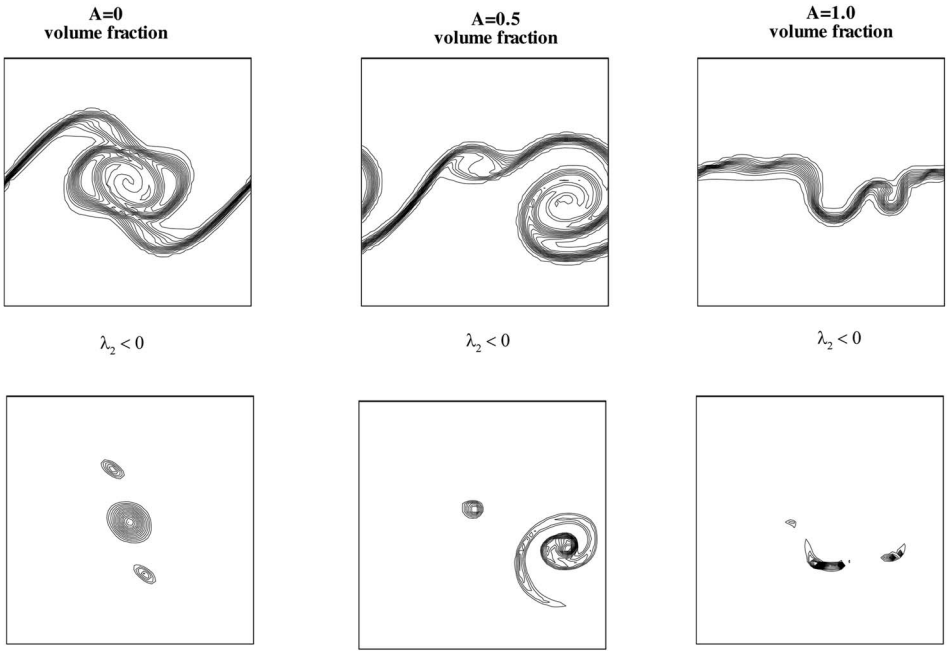

FIG. 7. Contours of volume fraction (top row) and negative second eigenvalue (bottom row) from 2D NS of a plane shear layer.

MAH-3 code [24] also show an increase of bubble velocities at late-time. The 2D NS of [22] suggest a strong correlation between bubble/spike curvature and their velocity variations. While the bubbles appear more pointed after the onset of acceleration in Fig. 1, the change in shape is less dramatic in the DNS calculations shown in Fig. 2. Thus, it is not evident if the bubble tip curvature is a determinant of the observed behavior reported here.

To eliminate numerics as a possible explanation of our observations, several tests were performed on the codes. First, the size of the domain was doubled to determine end wall effects, if any. Second, the MILES calculations were repeated at a higher resolution to reduce the effective numerical viscosity (details in the Appendix). Both these studies reproduced the results described above: Saturation velocity for $h_b/D_b < 1$ and bubble acceleration at late times. Finally, a numerical experiment was performed in which a buoyant spherical bubble was allowed to rise in a large container. The experiments of [14] report a constant value for the Froude number of a lenticular bubble of 2/3. Our simulations show a similar behavior, as the bubble rose self-similarly with a nearly constant Fr of 0.8. This suggests that the late-time acceleration observed for the RT bubble is not a result of numerical artifacts.

This acceleration of bubbles has not been reported in experiments of single-mode RT, since most experiments report bubble velocities up to $h_b/D_b \sim 1$. Planar laser induced fluorescence (PLIF) images from the drop-tank experiments of [15] show bubbles which appear square with an aspect ratio close to unity. The closest experimental analog to our calculations is the study of rising air bubbles in a long tube filled with water [14]. The authors of that paper who were interested in the question of how long it would take to empty such a tube of liquid report a constant Fr ~ 0.46 for the rising column of air. However, those experiments were at $A=1$, a regime in which we do not observe any acceleration either. Since these experiments had surface-tension effects, some of the high Atwood number DNS calculations were repeated with the addition of surface tension. These calculations showed only a slight decrease in the bubble acceleration with the inclusion of surface tension. We conclude this section by pointing out the need for single-mode RT experiments to study the late-time behavior of bubbles and spikes at all Atwood numbers.

IV. DISCUSSION: EFFECT OF SECONDARY INSTABILITIES

The coefficient C in (7) must describe various types of drag including form drag associated with the frontal area and friction drag associated with the total area of the bubbles. For instance, for a bluff object in wind tunnel flow, the total drag force may be written as [25]

$$F = \left\{ C_{\text{form}} \frac{D_b}{h_b} + 4 C_{\text{friction}} \frac{h_b}{D_b} \right\} h_b'^2 \frac{\rho_2}{\rho_1 + \rho_2} \frac{1}{h_b}. \tag{8}$$

Note that the above expression leads to a bubble acceleration at small aspect ratios (due to the form drag term) and a terminal velocity at large aspect ratios (due to the friction drag term). However, such a formulation by itself does not account for the Atwood number dependence of bubble acceleration observed in our simulations. We propose an explanation that includes form and friction drag effects, but also describes the change in bubble behavior due to changes in the density differences.

In this paper, we argue that at low-density differences, the formation of Kelvin-Helmholtz (K-H) rollups on the bubble-spike interface acts to accelerate the flow through two complementary mechanisms—reduction of the contact friction between bubbles and spikes and formation of a momentum jet due to induced flow that propels the bubbles forward. In the first scenario, K-H structures provide the rolling motion that mitigates the friction drag between bubbles and

spikes, similar to the friction-reducing action of such vortical structures caused by dimples on a golf ball. From (8), it is evident that while form drag is important for small bubble aspect ratios, it is the friction term that dominates the drag force late in time ($h_b/D_b \gg 1$). In the second scenario, the induced flow due to the K-H vortex ring creates a vertical momentum jet that propels the RT bubble forward. Such a "collimation of momentum" mechanism was proposed for the RT bubbles in a turbulent front in [26]. At large density differences, the Kelvin-Helmholtz instability is suppressed inertially, allowing the bubbles to coast with a terminal velocity.

We now proceed to give a more formal treatment to the ideas suggested above. First, the density effect on the linear and nonlinear growth of a shear layer is described here through 2D numerical simulations. The calculations were performed using RTI-3D in a square domain ($\lambda \times \lambda$), with periodic boundary conditions in the horizontal direction, and no-flux conditions in the direction of the velocity gradient. A velocity interface is established along the center of the domain, while the stream function is perturbed with a single wavelength. The velocity contrast between the two streams of fluid is spread over three numerical zones, corresponding to a piecewise linear velocity profile, while also ensuring the length scale of velocity variation is small in comparison to the perturbation wavelength. The shear velocities were chosen to be ±1 m/s. A sharp density contrast is superimposed on this background condition, and both positive and negative Atwood numbers were studied. Since, in the Rayleigh-Taylor flow, the shear force between bubbles and spikes and the buoyancy force driving the flow are orthogonal, our 2D shear calculations could be performed in the absence of gravity.

The top panel in Fig. 7 shows volume fraction contours at $A=0$, 0.5, and 1, respectively. It is necessary for our objectives to distinguish between the presence of vorticity with the formation of a vortex core in such flows (for instance, there is considerable vorticity at $A=1$ due to the large shear between the fluid streams, but no vortex). It is a K-H vortex (and not vorticity alone) that causes drag reduction in RT flows due to its rolling motion, and the resultant bubble acceleration. We use the definition of [27] who identify connected regions with two negative eigenvalues of the velocity gradient tensor, as a vortex. In other words, if $\lambda_1 \geqslant \lambda_2 \geqslant \lambda_3$ are the three eigenvalues of S^2+D^2, where S and D are the symmetric and antisymmetric components of the velocity gradient tensor, then a vortex core is a region with $\lambda_2 < 0$. This definition ensures that a vortex is a region of a pressure minimum while eliminating factors that cause false positives due to (a) unsteady straining and (b) viscous effects.

Contours of $\lambda_2 < 0$ are shown in the bottom panels of Fig. 7, and clearly demonstrate the presence of vortical structures at $A=0$ and 0.5, but none at $A=1$. As the flow is allowed to evolve later in time, the high-speed kinks observed in Fig. 7(f) are trapped in the low-speed stream (and vice versa) and are convected along with the slow-moving fluid. However, this happens late in time, is clearly a nonlinear effect, and does not result in the formation of vortex cores at $A=1$. In contrast, the vortex cores observed in Figs. 7(d) and 7(e) are the result of Kelvin-Helmholtz overturning early in time. Both the $A=0$ and $A=1$ cases were repeated with higher values of shear (2× and 4×). It was found that while the growth rate of the low density contrast cases scaled with ΔU, the infinite density difference case showed no variation with the velocity difference.

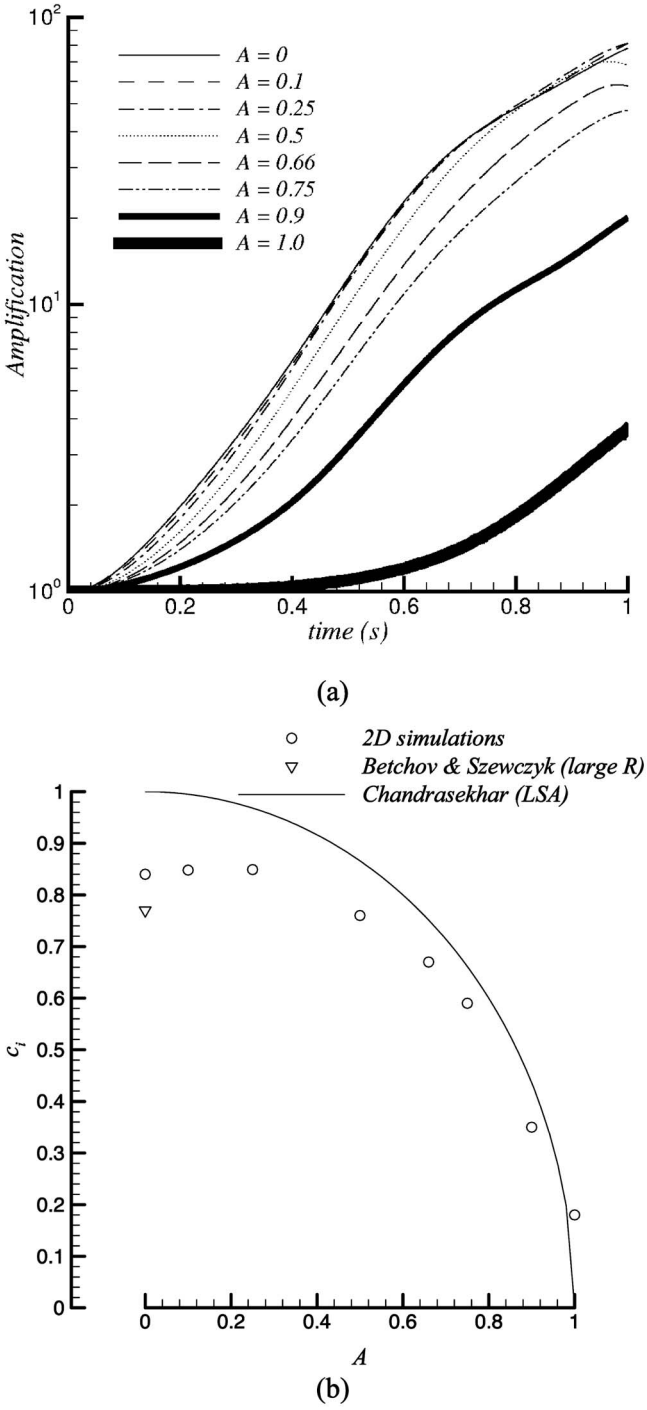

FIG. 8. (a). Amplification of centerline velocity fluctuations for the Kelvin-Helmholtz problem at different density differences and (b) the corresponding growth rates c_i as a function of A.

The growth rates of the shear layers in Fig. 7 may be quantified by the amplification of the rms vertical velocity fluctuations $\langle v'^2 \rangle / \langle v_0'^2 \rangle$ at the interface between the two fluids. Figure 8(a) is a semilogarithmic time history plot of the

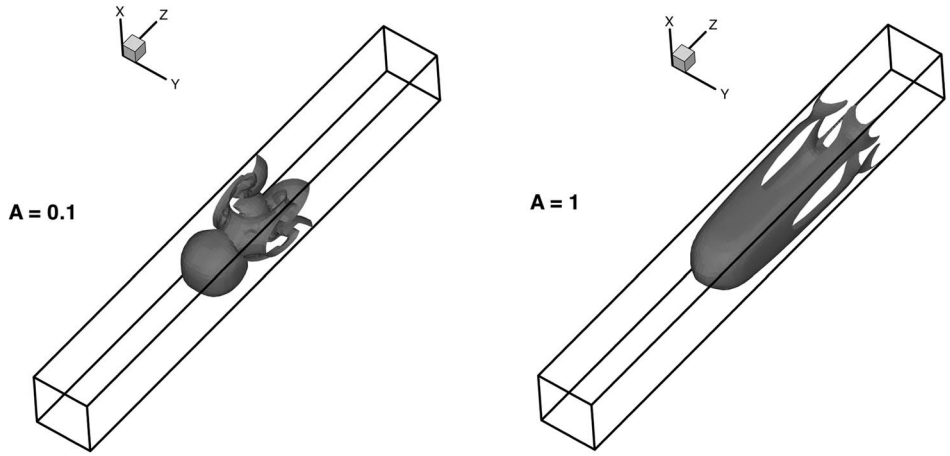

FIG. 9. Isosurfaces of volume fraction (=0.5) from the single-mode Rayleigh-Taylor calculations at $A=0.1$ (a) and $A=1$ (b).

amplification of velocity fluctuations at different density differences, and shows a consistent decay with increasing density contrasts. The late-time amplification observed for $A=1$ is a result of the nonlinear effect described above, and must be distinguished with the early onset of amplification seen in the other cases.

Growth rates deduced from Fig. 8(a) are shown in Fig. 8(b) as a function of the Atwood number. The linear stability analysis of [4] considers normal modes of the form $\exp i(k_x x+k_y y+c_i t)$, and obtains for the imaginary part of the growth rate, c_i, in the absence of surface tension and gravity

$$c_i = \pm \sqrt{-k_x^2(\Delta U)^2 \frac{\rho_1 \rho_2}{(\rho_1+\rho_2)^2}}. \tag{9}$$

The negative root of (9) results in exponential growth of perturbations, and shows good agreement with the numerically obtained growth rates in Fig. 8(b). Note that [4] considered a sharp velocity interface, while the numerical simulations were initialized with a piecewise linear velocity profile. However, care was taken to ensure that $k_x L \ll 1$, where L is the initial spread of the shear layer. In Fig. 8(b), we also compare the large-Reynolds number result of [28], who used a tangent hyperbolic initial velocity profile. Note that some calculations were also repeated with a reversal of the density gradient, which yielded growth rates identical to the standard cases, consistent with the symmetry of (9) with respect to ρ_1 and ρ_2.

We now revisit the 3D single-mode Rayleigh-Taylor (R-T) problem, with insight into the behavior of density effects on Kelvin-Helmholtz instabilities. Figures 9(a) and 9(b) are surfaces of $\rho=\frac{\rho_1+\rho_2}{2}$ from the R-T calculations at $A=0.1$ and 1.0, respectively, and clearly show the formation of vortical structure at low-density differences only. The realizations in Fig. 9 were chosen at times where the bubbles had penetrated to the same extent for both the low and high Atwood number simulations. Furthermore, our image analysis shows that at $A=1$, kinks similar to those observed in Fig. 7(e) form at the bubble-spike interface. For low A, the observed acceleration occurs when enough time t_{critical} has passed to allow for sufficient e foldings (n) of the Kelvin-Helmholtz instability, and this corresponds to $h_b/D_b \sim 1$. Equation (9) and Fig. 8(b) suggest that for $A \to 1$, $t_{\text{critical}} = n/c_i \to \infty$. From Fig. 8(b) it is also clear that for low A, c_i is only weakly dependent on A, and thus t_{critical} is roughly constant. This explains why the onset of acceleration is at $h_b/D_b \sim 1$.

Figure 10 shows the time history of the percentage volume of the computational domain that is occupied by vortices (identified through the condition $\lambda_2 < 0$), for $A=0.005$ and 1.0. The low Atwood number simulation shows a dramatic increase in this quantity close to $h_b/D_b \sim 1$, while the $A=1$ case shows no such trend.

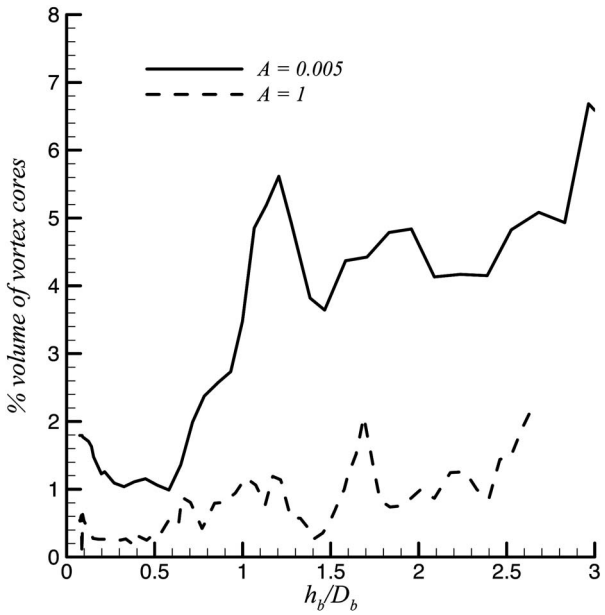

FIG. 10. Variation of vortex core size at $A=0.005$ and $A=1$ with the bubble aspect ratio.

V. SUMMARY

We have performed 3D numerical simulations using four different codes of a RT unstable single mode to the late-time regime $h_b/D_b \geq 1$ characteristic of the turbulent RT instability. The terminal velocity is found to depend on the value of A and h_b/D_b with the differences being attributed to a secondary instability similar to Kelvin-Helmholtz instability. The behavior has been observed in previous simulations [22–24] that extend to $h_b/D_b > 1$ but not in experiments [14,15] where $h_b/D_b < 1$ or where $A = 1$. The results are summarized as follows.

The behavior of the 3D single-mode simulations is quantified by plotting Fr scaled from Eq. (2) as the amplitude grows from the linear regime to $h_b/D_b \geq 2$. For $h_b/D_b \leq 1$, our numerical simulations obtain a terminal velocity with $\mathrm{Fr} \sim 0.56$ for all A, in agreement with potential flow theory [6] and drag-buoyancy models [5]. The subsequent behavior for $h_b/D_b > 1$ depends on A. For $A \sim 1$, Fr remains near 0.56 for all amplitudes consistent with potential flow. For $A < 1$, bubbles accelerate away from a terminal velocity, with the Fr approaching near unity as observed for individual RT bubbles in a chaotic flow [9,10,16] and for plumes [13] at $A \ll 1$. Due to limitations in computational capabilities and late-time unsteadiness due to secondary instabilities, we have not been able to determine conclusively what the asymptotic nature of this flow is under these conditions.

We examined two possible explanations for these observations. First, we considered a drag coefficient within the buoyancy-drag model which varies with the aspect (similarity) ratio of the bubble. This description allows for a reduced drag as the amplitude (aspect ratio) increased, but it does not explain the variation with Atwood number. Second, we considered the possibility that the reduced drag was due to appearance of vortical structures at the interface between the bubbles and spikes. This describes our variation with Atwood number since the linear growth rate of the Kelvin-Helmholtz instability vanishes as $A \to 1$. This was confirmed by performing 2D K-H simulations at various Atwood numbers.

We draw several tentative conclusions from these simulations. First, potential flow models are accurate in the regime that they are applicable, namely, for $A \sim 1$. Second, as A decreases, they lose accuracy at late times due to the onset of vortical motion which complicates the bubble shape, and this is outside their range of applicability—potential flow models [6] assume a simple parabolic shape for the bubble and solve for the flow immediately around the bubble tip. For $A < 1$, significant secondary vortices are generated and it can be described within the context of the growth of the K-H instability. The effect of the K-H vortex is twofold—(a) to reduce the friction drag between the bubbles and spikes, and (b) to propel the bubbles forward by concentrating a vertical momentum jet due to the induced flow. The first process can be understood by considering a wagon as a mechanical analogy. For $A \sim 1$, it appears that the wagon has no "wheels" (because K-H is stable and the drag is high). For $A < 1$, wheels are produced by the growth of the K-H instability and the associated drag is reduced. The second process is documented in the vortex dynamics literature [29], and is exploited by some species of fish to propel themselves. It has also been invoked as a mechanism of leading bubble acceleration [26] in the turbulent RT flow. More simulations and experiments with $[h_b/D_b > 1,\ A < 1]$ are needed to test and verify these hypotheses.

ACKNOWLEDGMENTS

P.R. and G.D. thank Malcolm J. Andrews for permitting the use of his computer program. The work at the Los Alamos National Laboratory was performed under the auspices of the U.S. Dept. of Energy (D.O.E) under Contract No. W-7405-ENG-36. Y.N.Y. thanks X. Lin, J. Glimm, and R. Rosner for helpful discussions. The NAV/STK code was developed by F. Ham and the simulations were conducted on the cluster at NJIT/DMS, funded by NSF/MRI. A.C. acknowledges support from the U.S. Department of Energy under Grant No. B523820 and to the Center for Astrophysical Thermonuclear Flashes at the University of Chicago. The FLASH software used in this work was developed in part by the DOE-sponsored ASC/Alliance Center for Astrophysical Thermonuclear Flashes at the University of Chicago. The PARAMESH software used in this work was developed at the NASA Goddard Space Flight Center under the HPCC and ESTO/CT projects.

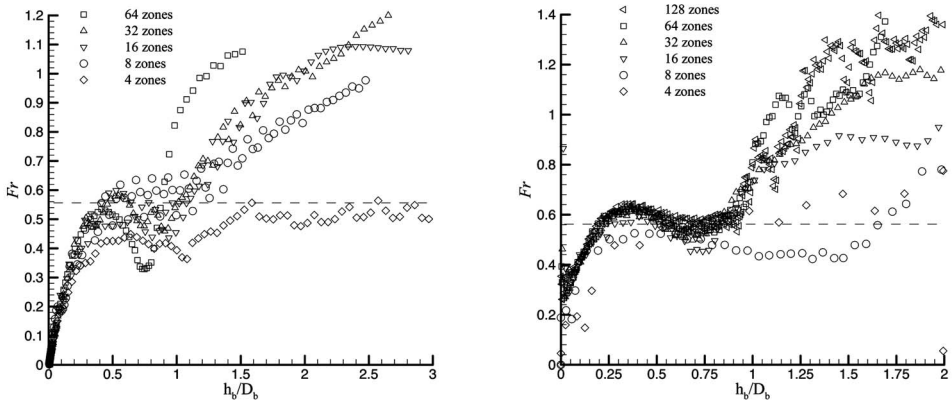

FIG. 11. Results of zoning study using RTI-3D (a) and FLASH (b). Plots show dependence of bubble Froude number as a function of aspect ratio.

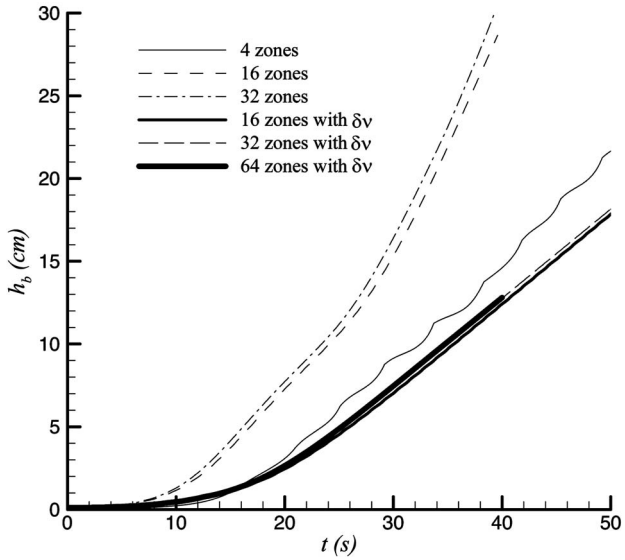

FIG. 12. Evaluation of numerical viscosity in the MILES codes: Plot shows that by adding a physical viscosity $\delta\nu$ given by (A1) to the high-resolution calculations, the highly diffusive result from 4 zones/λ is recovered. $A=0.1$.

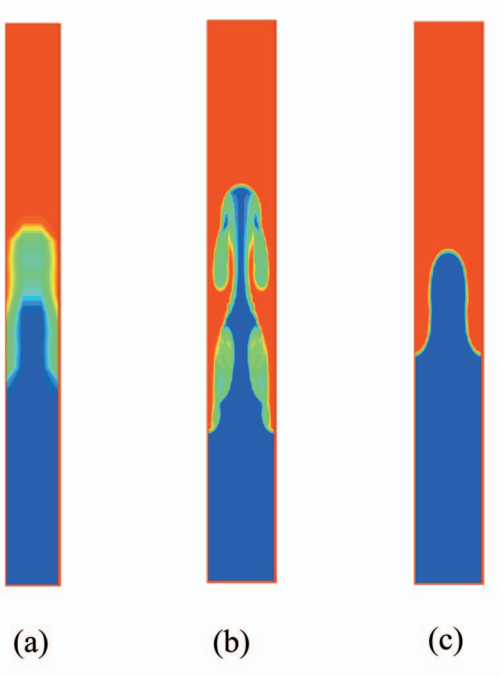

FIG. 13. (Color) Evaluation of numerical viscosity in the MILES codes: Volume-fraction contours at $t=30$ s from calculations with (a) 4 zones/λ, (b) 32 zones/λ, and (c) 32 zones/λ with $\delta\nu$ determined from (A1); $A=0.1$.

APPENDIX: NUMERICAL TESTS

To eliminate numerical resolution as a possible explanation for the observed effects, the calculations were repeated using RTI-3*D* at grid resolutions of 4, 8, 16, 32, and 64 zones across one wavelength. A similar zoning study was also undertaken using FLASH with grid resolutions of 4, 8, 16, 32, 64, and 128 zones across the domain. The results are plotted in Figs. 11(a) and 11(b), and show clearly that the effect is seen even at the highest grid resolution of 64 zones/λ and 128 zones/λ, respectively. Conversely, the bubble reacceleration is not seen at the poorest resolution of 4 zones/λ. At such a low resolution, the K-H secondary vortex does not develop [Fig. 13(a)], but is snuffed out by numerical viscous dissipation. This is similar to the suppression of high-wave number K-H modes at low Reynolds numbers due to physical viscosity, and is discussed in detail below.

We also performed the following test to characterize the numerical viscosity in some of our codes. As noted above, the poorly resolved calculations (4 zones/λ) do not exhibit the late-time acceleration, since the K-H instability is suppressed at such low (numerical) Reynolds numbers. This is in agreement with the nature of the dispersion curves for K-H [28], that show suppression of short wavelength modes at low Re (here, short wavelength modes are those wavelengths $\lambda_{\text{K-H}}<H$, where H is the initial shear layer width; for a grid resolution of 4 zones/λ, $H\sim\Delta$, and is larger than the most dominant K-H wavelength at that Re, which is suppressed as a result). We verify this by adding to a high-resolution calculation, in the form of a physical viscosity in the diffusion term, the additional numerical viscosity that a poorly-resolved calculation might have [estimated from (5)]. Thus, the 32 zones/λ calculation was repeated with an additional *physical* viscosity given by

$$\Delta\nu=\nu_{\text{numerical,4 zones}}-\nu_{\text{numerical,32 zones}}=\varpi\{\sqrt{Ag\Delta_{4\text{ zones}}^3}-\sqrt{Ag\Delta_{32\text{ zones}}^3}\}. \quad \text{(A1)}$$

The results are shown in Fig. 12, and demonstrate that with the additional viscosity $\Delta\nu$, determined self-consistently from (A1), the high-resolution calculations reproduce the behavior seen in the poorly-resolved calculation at 4 zones/λ, i.e., the bubble penetrations do not show a reacceleration at late times. The results from the high-resolution cases without $\Delta\nu$ are shown for comparison. The corresponding volume-fraction contours are plotted (at $t=30$ s) for the 4 zones/λ and the 32 zones/λ without and with $\Delta\nu$ in Figs. 13(a)–13(c), respectively. The high-resolution calculation with $\Delta\nu$ shows a sluglike structure similar to the poorly resolved case, suggesting that (a) the numerical viscosity is well characterized by (5), (b) that it is well behaved, and (c) that it mimics the action of physical viscosity with great fidelity. This is a demanding test for the numerical viscosity in our codes.

[1] Lord Rayleigh, *Scientific Papers II* (Cambridge University Press, Cambridge, England, 1900); G. I. Taylor, Proc. R. Soc. London, Ser. A **201**, 192 (1950).
[2] J. D. Lindl, *Inertial Confinement Fusion: The Quest for Ignition and Energy Gain Using Indirect Drive* (AIP, Woodbury, NY, 1998).
[3] S. F. Gull, Mon. Not. R. Astron. Soc. **171**, 263 (1975).
[4] S. Chandrasekhar, *Hydrodynamic and Hydromagnetic Stability* (Oxford University Press, Oxford, 1961).
[5] D. Oron *et al.*, Phys. Plasmas **8**, 2883 (2001).
[6] V. N. Goncharov, Phys. Rev. Lett. **88**, 134502 (2002).
[7] P. Ramaprabhu and Guy Dimonte, Phys. Rev. E **71**, 036314 (2005).
[8] Guy Dimonte, Phys. Rev. E **69**, 056305 (2004).
[9] Guy Dimonte and M. Schneider, Phys. Fluids **12**, 304 (2000).
[10] P. Ramaprabhu, Guy Dimonte, and M. J. Andrews, J. Fluid Mech. **536**, 285 (2005).
[11] J. Glimm *et al.*, Phys. Fluids A **2**, 2046 (1990).
[12] D. Shvarts *et al.*, Phys. Plasmas **2**, 2465 (1995).
[13] R. S. Scorer, J. Fluid Mech. **2**, 583 (1957).
[14] R. M. Davies and G. I. Taylor, Proc. R. Soc. London, Ser. A **200**, 375 (1950).
[15] J. T. Waddell, C. E. Niederhaus, and J. W. Jacobs, Phys. Fluids **13**, 1263 (2001).
[16] Guy Dimonte *et al.*, Phys. Fluids **16**, 1668 (2004).
[17] M. J. Andrews, Int. J. Numer. Methods Fluids **21**, 205 (1995).
[18] B. Fryxell *et al.*, Astrophys. J., Suppl. Ser. **131**, 273 (2000); A. C. Calder *et al.*, *ibid.* **143**, 201 (2002).
[19] B. Fryxell, E. Müller, and D. Arnett, Hydrodynamics and Nuclear Burning (MPI Astrophys. Rep. 449; Garching: MPI Astrophys.).
[20] P. MacNiece, K. M. Olson, C. Mobary, R. deFainchtein, and C. Packer, Comput. Phys. Commun. **126**, 330 (2000).
[21] L. Duchemin, C. Josserant, and P. Clavin, Phys. Rev. Lett. **94**, 224501 (2005).
[22] J. Glimm, X. L. Li, and A-D. Lin, Acta Math. Appl. Sin. **18**, 1 (2002).
[23] Y-N. Young *et al.*, J. Fluid Mech. **447**, 377 (2001).
[24] N. N. Anuchina *et al.*, J. Comput. Appl. Math. **168**, 11 (2004).
[25] S. F. Hoerner, *Fluid Dynamic Drag*, 1965.
[26] N. A. Inagamov *et al.*, J. Exp. Theor. Phys. **92**(4), 715 (2001).
[27] J. Jeong and F. Hussain, J. Fluid Mech. **285**, 69 (1995).
[28] R. Betchov and A. Szewczyk, Phys. Fluids **6**, 1391 (1963).
[29] F. E. Fish and G. V. Lauder, Annu. Rev. Fluid Mech. **38**, 192 (2006).